Received: 18 January 2022 | Revised: 12 March 2022 | Accepted: 30 March 2022

DOI: 10.1002/sus2.61

RESEARCH ARTICLE

SusMat WILEY

Boosting the energy density of aqueous MXene-based supercapacitor by integrating 3D conducting polymer hydrogel cathode

Xiang Chu[1,2] | **Yihan Wang**[1] | **Lucheng Cai**[1] | **Haichao Huang**[1] | **Zhong Xu**[1] | **Yanting Xie**[1] | **Cheng Yan**[1] | **Qing Wang**[1] | **Haitao Zhang**[1] | **Hong Li**[2] | **Weiqing Yang**[1]

[1]Key Laboratory of Advanced Technologies of Materials, Ministry of Education, School of Materials Science and Engineering, Southwest Jiaotong University, Chengdu, P. R. China

[2]School of Mechanical and Aerospace Engineering, Nanyang Technological University, Singapore, Singapore

Correspondence
Weiqing Yang, Key Laboratory of Advanced Technologies of Materials, Ministry of Education, School of Materials Science and Engineering, Southwest Jiaotong University, Chengdu 610031, P. R. China.
Email: wqyang@swjtu.edu.cn

Xiang Chu, Yihan Wang, and Lucheng Cai contributed equally to this work.

Funding information
National Natural Science Foundation of China, Grant/Award Numbers: 51977185, 51972277; Sichuan Science and Technology Program, Grant/Award Numbers: 20ZDYF2478, 20ZDYF2833, 21ZDYF3951

Abstract

The wide-spread proliferation of aqueous MXene-based supercapacitor has been largely shadowed by the limited cell potential window (typically in the range of 0–0.6 V). To address this baffling issue, designing asymmetric supercapacitor (ASC) is proposed as a rational strategy to enlarge the potential window (thus energy density) of individual cell in aqueous electrolytes. To this date, however, it still remains a great challenge to develop easy fabricating, 3D nanostructured, and pseudocapacitive cathode materials that can perfectly match with MXene anode materials. In this work, we propose a supramolecular strategy to construct conducting polymer hydrogel (CPH) with highly interconnected 3D nanostructures and large pseudocapacitance, which can finely match with 2D $Ti_3C_2T_x$. The as-assembled CPH//$Ti_3C_2T_x$ ASC with CPH cathode and MXene anode can operate in a broadened potential window of 1.15 V in aqueous PVA/H_2SO_4 gel electrolyte with remarkably improved energy density of 16.6 μWh/cm^2 (nine times higher than that of symmetric MXene supercapacitor). Additionally, this ASC exhibits outstanding cyclic stability with no trackable performance decay over 30,000 galvanostatic charge and discharge cycles. It is demonstrated in this work that employing positive CPH electrode is a feasible yet promising strategy to enhance the potential window and energy density of aqueous MXene supercapacitors.

KEYWORDS
conducting polymer hydrogel, electrochemical energy storage, electrochemical polymerization, high energy density, MXene

1 | INTRODUCTION

Two-dimensional (2D) carbides and nitrides of transition metals, also known as MXenes, have attracted extensive research interests in the past decade since the discovery of Ti_3C_2 in 2011.[1–3] In general, the widely recognized formula of MXenes can be denoted as $M_{n+1}X_nT_x$ (n = 1-3), where M represents transition metal (such as Sc, Ti, Nb, and so on), X represents carbon and/or nitrogen, and T_x stands for the surface terminations including hydroxyl, oxygen, and fluorine.[4–6] Typically, MXene layers can be obtained through a top-down synthesis routine, in which the A-layer atoms in MAX phase are selectively removed by either harsh or mild etching.[7–9] To this date, MXene has become a starring role in electrochemical energy storage due to its high electronic conductivity,[10,11] easy processing (allow spray coating,[12,13] ink-jet printing,[14–16] screen printing,[17,18] and 3D printing[19–21]), and high pseudocapacitance originated from abundant surface terminations.[22–24] MXene generally shows promising electrochemical activity under negative potential in aqueous acidic electrolytes. However, the widespread application of MXene-based symmetric supercapacitor is largely shadowed by the limited potential window of individual cell in aqueous acidic electrolytes (typically in the range of 0–0.6 V).[13,25] Therefore, it is of great urgency to broaden the potential window of MXene-based aqueous supercapacitors considering practical application and commercialization of devices.

Designing asymmetric supercapacitor (ASC) is a rational strategy to enhance the potential window (thus energy density) of MXene-based supercapacitor in aqueous acidic electrolyte.[26–28] For instance, Yury and his co-workers developed rGO//MXene ASC, which demonstrates a potential window of 1 V in aqueous PVA/H_2SO_4 electrolyte.[29] Although positive rGO electrode can effectively broaden the potential window of individual cell in acidic electrolyte, it cannot perfectly match negative MXene electrode in specific capacitance due to the lack of redox-induced pseudocapacitance. Soon after this work, Yury's group developed conducting polymer (CP)@rGO composite cathode material for MXene. The resultant CP@rGO//MXene ASC delivers an unprecedented potential window of 1.45 V in acidic electrolyte.[30] In spite of the ultrahigh potential window, the long-term performance of device is inevitably compromised due to the interfaces between CP and rGO. Additionally, the 3D nanostructure of CP@rGO cathode material obtained by diluted solution polymerization cannot be enabled due to the restacking of rGO flakes, which will lead to sluggish ion/mass transfer kinetics.[31–33] In this regard, developing easy fabricating, 3D-nanostructured, and pseudocapacitive cathode materials that can perfectly match with MXenes anode is still underway.

CP hydrogels (CPHs) represent an emerging class of derivative of CPs that synergize the advantages of soft hydrogels and organic conductors.[34–36] Due to the intrinsic 3D architecture, large pseudocapacitance, promising mechanical durability, and easy fabricating, CPHs have recently gained ground in high performance supercapacitors.[37,38] Moreover, CPHs generally show considerable electrochemical performance in aqueous acidic electrolyte under positive potential, which makes them ideal cathode materials for MXene-based ASC.[39,40] Herein, we construct 3D CPH through crosslinking polyaniline (PANI) chains with citric acid (CA) via electrochemical polymerization. The CPH consisting of numerous interconnected nanofibers offers interconnected and unblocked channels for ion/mass transfer during electrochemical process. Thanks to this unique 3D architecture, the CPH demonstrates a high specific capacitance of 402.5 F/g at 1 A/g under positive potential (0–0.8 V) in acidic electrolytes. Through employing CPH cathode and MXene anode, a CPH//$Ti_3C_2T_x$ ASC is successfully assembled with a broadened potential window of 1.15 V in acidic gel electrolyte. In the meanwhile, the CPH//$Ti_3C_2T_x$ ASC demonstrates remarkably enhanced energy density of 16.6 μWh/cm^2, which is nine times higher than that of symmetric MXene supercapacitor. This work demonstrates a novel MXene-based ASC prototype, which may give inspirable insights into next-generation high-energy density electrochemical energy storage devices.

2 | EXPERIMENTAL SECTION

2.1 | Chemicals and materials

Aniline, CA monohydrate, and polyvinyl alcohol (PVA) with 1799 degree of polymerization of analytical grade were purchased from Aladdin Co., Ltd. and aniline was distilled under reduced pressure before using. Hydrochloric acid (HCl), sulfuric acid (H_2SO_4), and lithium fluoride (LiF) were purchased from Chengdu Chron Chemicals Co., Ltd., China. The Ti_3AlC_2 MAX phase powder is purchased from 11 Technology Co., Ltd., Jilin, China. Polydimethylsiloxane (PDMS) was purchased from Dow Corning Ltd. (USA) and used as received without further treatment.

2.2 | Preparation of MXene ink

The preparation procedure of MXene ink has been described in detail in our previous work.[8] Generally, the $Ti_3C_2T_x$ powder was prepared by etching Ti_3AlC_2 MAX phase in acidic environment containing HCl and LiF. The obtained multilayer $Ti_3C_2T_x$ powder was dispersed in

deionized water (10 mg/mL), followed by ultrasonic treatment (120 W) for 1 h. After that, the dark supernatant liquid was collected by centrifugation treatment at 3500 rpm for 1 h, which is so-called MXene ink. To point it out, the concentration of the MXene ink we used for spray coating is tested to be 2.4–2.5 mg/mL by determining the solid content of this ink.

2.3 | Electrochemical polymerization of 3D CPH

Commercialized polyethylene terephthalate (PET) thin film (75 μm) was cut into small pieces (40 mm × 15 mm) and rinsed with ethanol and deionized water for three times, respectively, to remove contaminants. Gold thin film with predesigned patterns was then sputtered onto the PET film using magnetron sputtering apparatus (SKY Technology Development Co., Ltd., China). A precursor solution was prepared by adding 912 μL (10 mmol) aniline and 1.0507 g (5 mmol) CA monohydrate into 100 mL 1 M H_2SO_4 solution. Then, the gold foil patterned PET slice (working electrode) was integrated into three-electrode configuration for the following electrochemical polymerization, in which platinum foil and saturated calomel electrode (SCE) were employed as counter electrode and reference electrode, respectively. For a typical fabrication of CPH, the above-mentioned three-electrode configuration is dipped into precursor solution, and a fixed potential of 0.8 V versus SCE was applied onto the working electrode. The CPH can, thus, be gradually formed with time. To point it out, the aniline concentration of the precursor solution is 0.1 mol/L, and the molar ratio between aniline and CA is 2:1.

2.4 | Fabrication of asymmetric supercapacitor (ASC)

Positive CPH electrode was prepared by electrochemical polymerization at a fixed potential of 0.8 V versus SCE. Negative MXene electrode was prepared by a mask-assisted spray coating method using MXene ink. PVA/H_2SO_4 gel electrolyte was prepared by mixing PVA, concentrated sulfuric acid, and deionized water (mass ration of 10:1:1) at an elevated temperature of 85°C for 2 h. Notably, during the preparation of positive and negative electrodes, the employment of binder and conductive agent can be effectively avoided, which is attributed to the promising conductivity and processability of both CPH and MXene. To assemble a CPH//$Ti_3C_2T_x$ ASC, positive CPH electrode (cathode), PVA/H_2SO_4 gel electrolyte, and negative MXene electrode (anode) were integrated in a sandwiching manner, in which the gel electrolyte is sandwiched in between the two electrodes. To achieve the charge balance of $Q^+ = Q^-$, a mass balance equation is employed to enable the optimized electrochemical performance of ACS:

$$m_+ C_{electrode+}\, \Delta E_+ = m_-\, C_{electrode-} \Delta E_-, \tag{1}$$

where m^+, and m^- is the loading mass of CPH and MXene electrode, respectively. $C_{electrode+}$, and $C_{electrode-}$ is the specific capacitance of CPH and MXene, respectively. ΔE_+, and ΔE_- is the potential window of each electrode. After the electrodes and gel electrolyte are properly assembled, PDMS is drop casted onto the device, serving as encapsulating layer.

2.5 | Materials characterization

Scanning electron microscopy (SEM) of materials was characterized with JSM-7800F Prime (JEOL Co. Ltd., Japan) using an accelerating voltage of 5 kV at high vacuum mode (9.6×10^{-5} Pa). Transmission electron microscopy (TEM) was conducted on JEM-2100F (JEOL Co. Ltd.) with an accelerating voltage of 200 kV. Fourier transformed infrared (FTIR) spectra of CPH and pure PANI were characterized by Nicolet 6700 spectrometer (Thermo Fisher Scientific, US). Raman spectra of dehydrated CPH, pure PANI, and MXene were characterized using LabRAM HR Evolution (HORIBA Instruments Shanghai Co. Ltd., China). X-ray diffraction (XRD) of the specimens were tested with PANalytical X'Pert Powder diffractometer with Cu Kα radiation. X-ray photoelectron spectroscopy (XPS) was conducted on Thermo Scientific ESCALAB 250Xi.

2.6 | Evaluation and determination of electrochemical performance

Electrochemical performance of electrode materials was tested in a prototypical three-electrode configuration, in which 1 M H_2SO_4 solution was employed as electrolyte, platinum film and SCE were used as counter electrode and reference electrode, respectively. Electrochemical performance of as-assembled ASC was tested in two-electrode system using CHI660E electrochemical workstation. Specific capacitance (F/g) of electrochemical active materials is derived from galvanostatic discharge technique:

$$C_s = I\Delta t / m\Delta E, \tag{2}$$

where I (A) is discharge current, Δt (s) is discharge time, m (g) is the loading mass of electrochemical active material, and ΔE (V) is potential window.

Areal capacitance (C_A, F/cm^2) of device is calculated by the following equation:

$$C_A = C_{device}/A, \tag{3}$$

where C_{device} (F) is the device capacitance and A (cm^2) is the effective areal of device.

Energy density (E, Wh/cm^2) of as-prepared ASC can be calculated according to:

$$\mathrm{E} = \frac{1}{2} C_A \frac{(\Delta V)^2}{3600}. \tag{4}$$

Power density (P, W/cm^2) of as-prepared ASC can be calculated according to:

$$\mathrm{P} = \frac{E}{\Delta t} \times 3600. \tag{5}$$

3 | RESULTS AND DISCUSSION

The main idea of this work is schematically illustrated in Figure 1. It is widely recognized by academia that MXenes show promising electrochemical performance in acidic electrolyte under negative potential. However, the limited potential window of MXene-based symmetric supercapacitors in aqueous acidic electrolyte severely hinders their wide application and proliferation. To address this baffling issue, we employ here the CPH cathode in an attempt to broaden the potential window of MXene-based supercapacitors. The 3D CPH is constructed via a supramolecular strategy, in which PANI polymeric chains are successfully crosslinked by CA molecules due to electrostatic interaction and hydrogen bond. Since pseudocapacitive CPH cathode shows promising electrochemical performance in acidic electrolyte under positive potential, it can perfectly match MXene anode that works under negative potential. As a result, the as-fabricated CPH//$Ti_3C_2T_x$ ASC exhibits a remarkably enlarged potential window of 1.15 V, which is much larger than that of MXene-based symmetric supercapacitor (0.6 V).

The supramolecular strategy we employed to synthesize CPH is clearly illustrated in Figure 2A. For a typical fabrication of CPH, aniline, and CA were added into precursor solution, followed by an electrochemical polymerization method (see details in Materials and Methods). In this supramolecular strategy, the CA molecule plays a dual role of both crosslinker and dopant. On one hand, PANI polymeric chains can be doped by acidic carboxyl groups of CA. On the other hand, hydrogen bond can be formed between carboxyl groups of CA and imine groups of PANI. Since every CA molecule possesses three functional groups, it can crosslink more than one PANI macromolecular chains. Consequently, a 3D interconnected CPH network consisting of numerous nanofibers comes into formation. To point it out, the loading mass of CPH can be strictly controlled through varying the electrochemical polymerization time because the loading mass of CPH increases proportionally with the reaction time (Supplementary Figure S1). The loading mass of CPH deposited on individual electrode is tested to be 0.03 mg/cm^2 with an electrochemical polymerization time of 120 s. Increasing the electrochemical polymerization time to 600 s leads to the loading mass tested to be 1.04 mg/cm^2. With the prolongation of polymerization time, the color of electrode changes from light brown to dark green, which indicates an increment in loading mass (Supplementary Figure S2). Top view SEM image of as-prepared CPH is shown in Figure 2B. It can be clearly observed that this CPH consists of numerous interconnected nanofibers, and the average diameter of PANI/CA fiber is calculated to be 55 nm (Supplementary Figure S3). EDS mapping of CPH in Figure 2C suggests even distribution of carbon, nitrogen, and oxygen element, which is consistent with the chemical structure shown in Figure 2A. Cross-section SEM image of CPH grown on gold (Au) thin film is depicted in Figure 2D, which shows a distinct three-layer structure, containing substrate (bottom layer), Au film (medium layer), and CPH (top layer). It is noteworthy that the average fiber diameter in the cross-section SEM image (160 nm) seems to be much larger than that (55 nm) in top view SEM image (Supplementary Figure S4). This is attributed to the secondary growth of PANI. During the electrochemical polymerization process, the CPH starts growing at the surface of Au film. Therefore, the fibers near Au film endure longer polymerization time and appear to be thicker than that on the top of CPH. Notably, the CPH layer is closely adhered onto the Au film without trackable delamination. Therefore, the redox current contributed by CPH can be fully collected by the Au film during the electrochemical procedure, and promising electrochemical performance can be obtained consequently.

FTIR spectrum is employed to probe the chemical structure of as-prepared CPH (Figure 2E). A reference scan of pure PANI in dedoped state is also depicted in Figure 2E for comparison. In the spectrum of CPH, the characteristic peaks located at 1560, 1491 cm^{-1} are corresponded to the C = C stretching vibration of quinoid and benzenoid ring, respectively.[41] The peak located at 1301 cm^{-1} is attributed to the C-N stretching vibration of imine group of PANI backbone, and the peak of 1140 cm^{-1} is attributed to the C = N

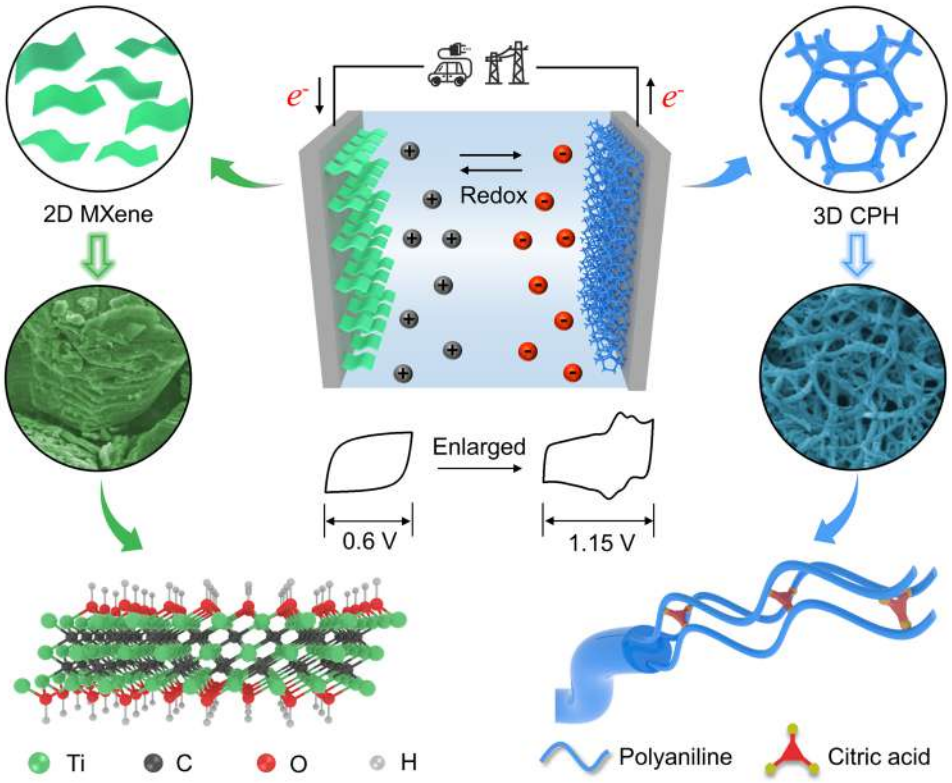

FIGURE 1 Schematic illustration of designing CPH//$Ti_3C_2T_x$ ASC by integrating CPH cathode and $Ti_3C_2T_x$ MXene anode, in which MXene is obtained by etching MAX phase, and CPH is constructed via crosslinking PANI polymeric chains. Compared with symmetric MXene supercapacitor (0.6 V), the potential window of CPH//$Ti_3C_2T_x$ ASC can be efficiently broadened to 1.15 V

stretching vibration of -N = Q = N- unit (Q represents quinoid ring). As for the peak of 820 cm^{-1}, it is assigned to the out-of-plane bending vibration of C-H bond located in benzenoid ring. All these above-mentioned characteristic peaks confirmedly demonstrate the existence of PANI. Due to the presence of CA molecules, the peak located at 1560 cm^{-1} in CPH spectrum appears to be broader than that of pure PANI (due to the overlap of –COOH carbonyl functionality peak and quinoid ring C = C stretching vibration peak). Notably, the distinct red shift phenomenon appeared in the CPH spectrum indicates the PANI polymeric chains are effectively doped by CA molecules. In the Raman spectra of pure PANI and CPH (Figure 2F), the peaks located at 417, 812, and 1603 cm^{-1} are ascribed to the fundamental vibrations of benzenoid ring. The peaks at 1494 cm^{-1} (C = C and C = N stretching vibrations of quinoid ring) and 1170 cm^{-1} (C-H deformation vibration of quinoid ring) indicate the presence of quinoid ring. Additionally, the peak at 570 cm^{-1} is ascribed to the amine deformation vibration, and the peak at 1333 cm^{-1} is ascribed to the C-$N^{\bullet+}$ stretching vibration of delocalized polaron structure.[42] Both, the FTIR and Raman spectra demonstrate that the PANI polymeric chains have been successfully doped by CA molecules. Due to the high doping level of PANI polymeric chains, the CPH exhibits high electronic conductivity of 0.45 S/cm (tested by a standard four-probe testing method).

Chemical composition of as-prepared CPH was further determined by XPS characterization, which indicates the presence of carbon (C1s~284 eV), nitrogen (N1s~399 eV), and oxygen (O1s~531 eV) (Supplementary Figure S5). According to the quantitative elementary analysis, the carbon, nitrogen, and oxygen element were calculated to be 73.9, 7.7, and 16.7%, respectively. The high concentration of oxygen is attributed to the introducing of CA molecules. Deconvoluted XPS core-level spectra of N (1s) is shown in Fiugre 2G, in which the peak of –N = is located at 398.3 eV, the peak of –NH- is located 399.2 eV, and the peak of $–N^+$ is located at 400.5 eV. The high doping level (35.3%, -N+/overall N element) of PANI polymeric chains revealed by XPS N (1s) spectrum is consistent with FTIR and Raman results. As for the C (1s) spectra of the CPH (Supplementary Figure S6), it can be deconvoluted into four peaks: the C-C/C-H peak is centered at 284.1 eV, the C-N/C = N peak is centered at 284.9 eV, the C-N^+/C = N^+ peak is centered at 285.6 eV, and the C-O/C = O peak is centered at 288.7 eV. XRD pattern of hydrated CPH (Supplementary Figure S7) shows two characteristic diffraction

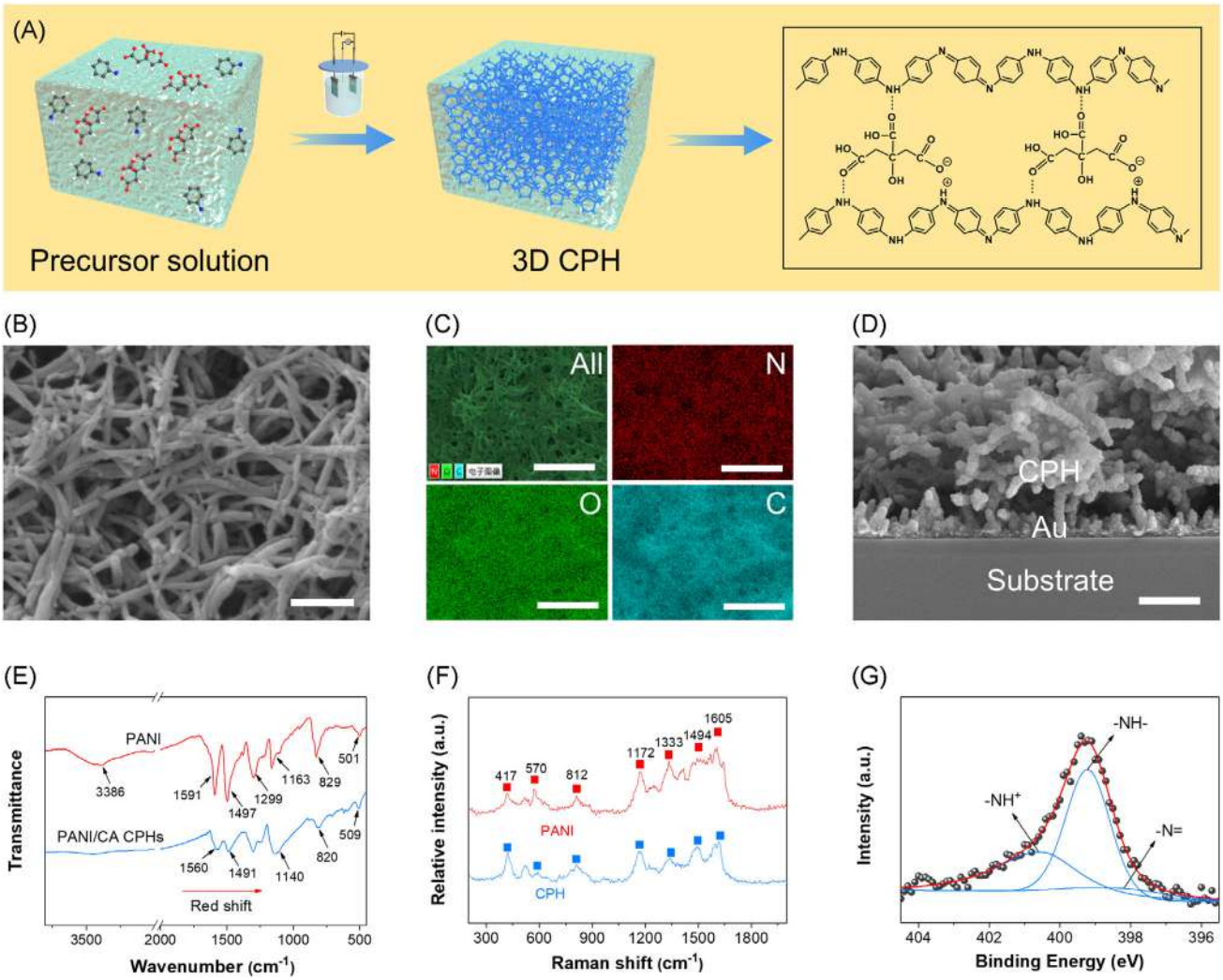

FIGURE 2 Synthesis and characterization of CPH. (A) Electrochemical polymerization of CPH. (B) SEM image of dehydrated CPH, scale bar: 500 nm. (C) EDS mapping of dehydrated CPH, scale bars: 1 μm. (D) Cross-section SEM image of dehydrated CPH deposited onto substrate, scale bar: 1 μm. (E) FTIR, and (F) Raman spectra of pure PANI and dehydrated CPH. (G) N 1s deconvoluted spectra of dehydrated CPH

peaks located at 2 theta degree of 19.7° and 25.0°, which are assigned to (0 2 0) and (2 0 0) crystal planes diffraction of PANI in emeraldine base.

As vividly shown in Figure 3A, $Ti_3C_2T_x$ MXene ink is typically prepared by etching Ti_3AlC_2 MAX phase, followed by a sequential dispersing procedure. As a result, the obtained MXene layers exhibit considerable hydrophilicity, and the MXene ink, thus, shows distinct Tyndall effect (inset of Figure 3A). AFM image of dehydrated $Ti_3C_2T_x$ MXene ink is shown in Figure 3B. The thickness of MXene monolayer is determined to be 1.9–2.2 nm by AFM characterization (see height profiles in Figure 3C). Cross-section SEM image of negative MXene electrode is depicted in Figure 3D. A distinct three-layer structure can be clearly observed in the SEM image, in which the bottom layer is substrate, the middle layer is sputtered Au film, and the top layer is laminated porous MXene electrodes. As shown in Figure 3E, TEM image of dehydrated MXene ink indicates it is mainly composed of single-layered MXene flakes with mean lateral size less than 1 μm. Such a small mean lateral dimension of MXene flakes can be attributed to the vigorous ultrasonic treatment. Generally speaking, the small lateral size and large interlayer space of MXene flakes can facilitate ion accommodation and inter-layer ion transfer, which will alleviate sluggish ionic kinetics of MXene film to a certain extent (Supplementary Figure S8). The lattice symmetry of selected area electron diffraction (SAED) pattern of MXene flake is in good agreement with previous literatures.[43] Raman spectrum of MXene powder is exhibited in Figure 3F. The sharp peaks of 201 and 722 cm^{-1} are typical indicators of delaminated $Ti_3C_2T_x$ MXene, which are assigned to the vibration modes of A_{1g}

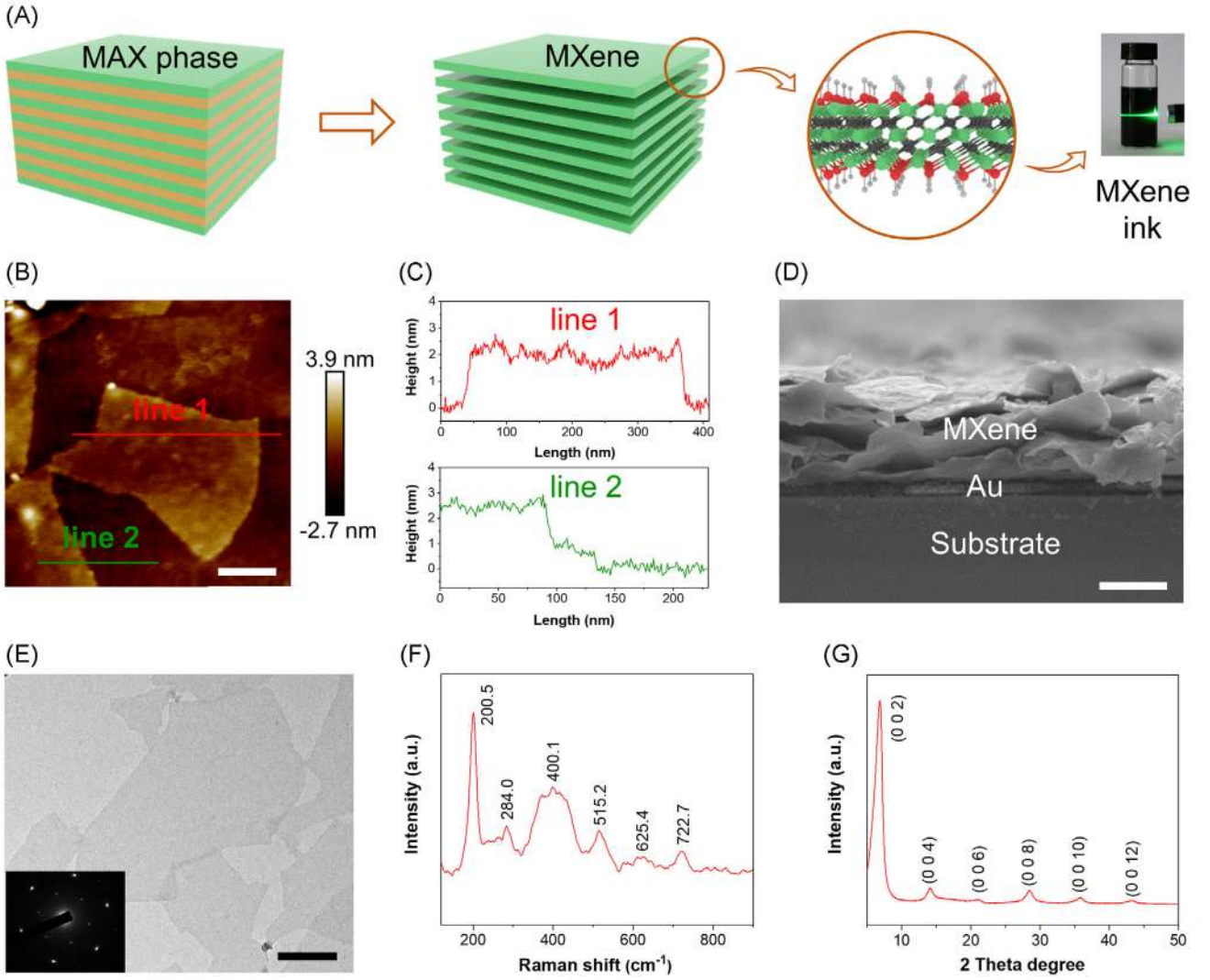

FIGURE 3 Synthesis and characterization of $Ti_3C_2T_x$ MXene. (A) MXene flakes can be facilely fabricated by etching MAX phase. (B) AFM image of MXene monolayers, scale bar: 110 nm. (C) Height profiles of MXene monolayers along the crossed lines. (D) Cross-section SEM image of MXene electrode, scale bar: 1 μm. (E) TEM image shows few-layered MXene flakes, scale bar: 200 nm. Inset picture is SAED pattern. (F) Raman spectra of MXene powder. (G) XRD pattern of as-prepared $Ti_3C_2T_x$ MXene

(Ti, O, C) and A_{1g} (C).[44,45] The bands of 515 and 625 cm^{-1} are attributed to the out-of-plane and in-plane vibration modes of $Ti_3C_2(OH)_2$, respectively.[46] XRD pattern of as-etched MXene is depicted in Figure 3G, the sharp peak located at 6.9° is assigned to the diffraction of (002) crystalline plane of MXene. The peaks centered at 14.1°, 21.2°, 28.5°, 35.9°, and 43.0° are attributed to the diffraction of (004), (006), (008), (0010), and (0012) planes of MXene.[11]

To investigate the electrochemical performance of as-prepared $Ti_3C_2T_x$ MXene and CPH, electrochemical tests were conducted with three-electrode configuration in 1 M H_2SO_4 electrolyte. As a result, the $Ti_3C_2T_x$ MXene shows promising electrochemical performance of 213.8 F/g under the potential window of -0.35-0.3 V versus SCE (Supplementary Figure S9). While the CPH delivers high specific capacitance of 402.5 F/g with a potential window of 0–0.8 V versus SCE (Supplementary Figure S10). Consequently, an ASC can be easily assembled in a sandwiching manner by integrating CPH cathode, MXene anode, and acidic gel electrolyte (Figure 4A). As shown in Figure 4B, due to the large open channels of 3D CPH and abundant interlayer space of 2D MXene, the solvated ions can easily accommodate into nanostructured electrodes and, thus, achieve efficient electrochemical dynamics. Figure 4C shows the cyclic voltammetry (CV) curves of each individual electrode (20 mV/s) recorded in three-electrode configuration, in which the negative electrode ($Ti_3C_2T_x$ MXene) works at -0.35–0.3 V while the positive electrode (CPH) works at 0–0.8 V. This indicates the possibility to enlarge the overall potential window of individual cell by assembling CPH//$Ti_3C_2T_x$ ASC. CV curves of as-assembled CPH//$Ti_3C_2T_x$ ASC with different

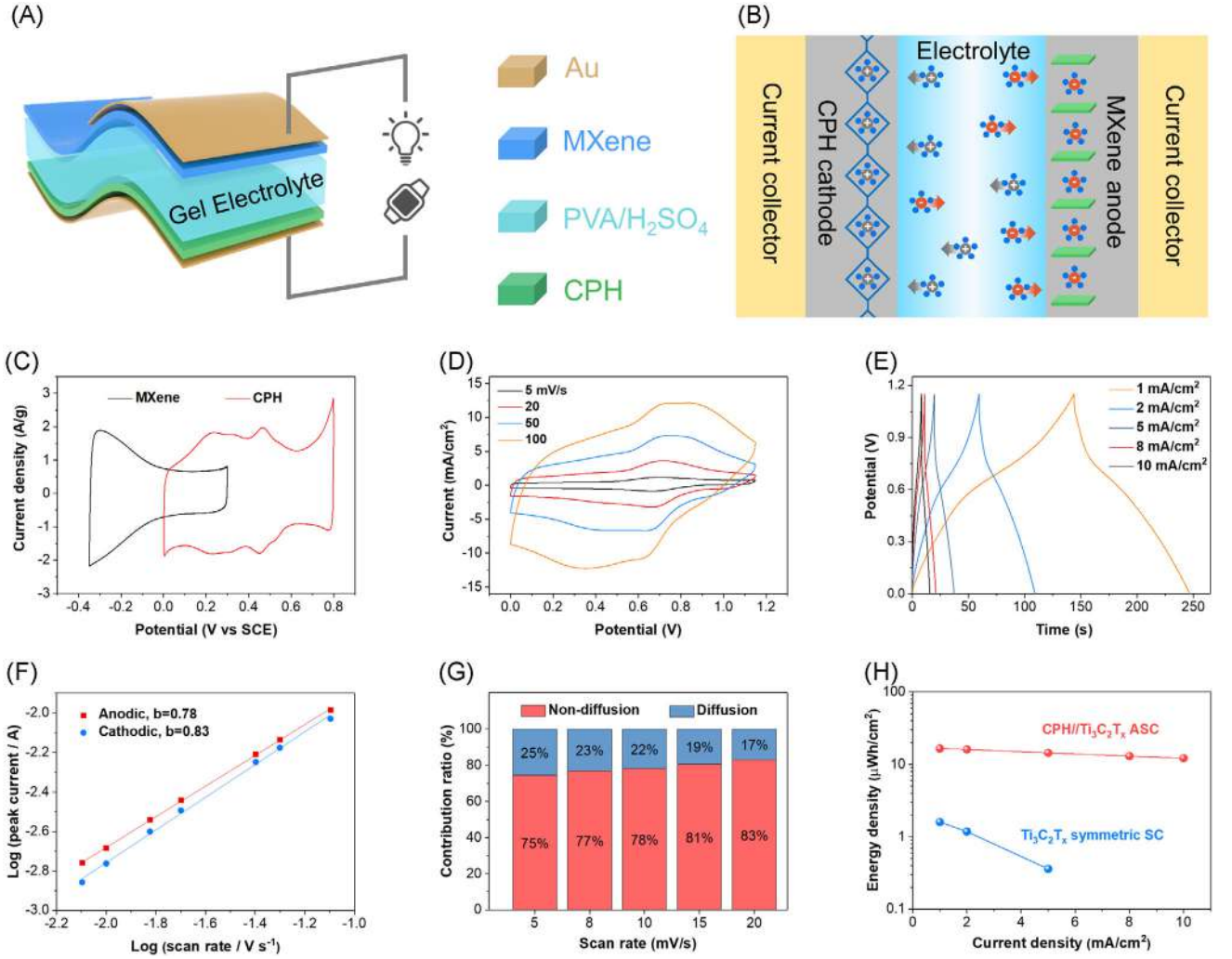

FIGURE 4 Electrochemical performance of CPH//$Ti_3C_2T_x$ ASC. (A) The CPH//$Ti_3C_2T_x$ ASC is assembled in a sandwiched manner. (B) The large open channels of CPH and abundant interlayer space of MXene can facilitate ion or mass transfer. (C) CV curves of individual electrode of $Ti_3C_2T_x$ MXene and CPH tested in three-electrode system, (D) CV and (E) GCD curves of as-assembled CPH//$Ti_3C_2T_x$ ASC. (F) The *log(i)* versus *log(v)* plot of the cathodic and anodic peak current of CV curves. (G) Quantitative survey of diffusion and non-diffusion-limited current contributions at different scan rates of 5–20 mV/s. (H) The energy density of CPH//$Ti_3C_2T_x$ ASC and $Ti_3C_2T_x$ symmetric supercapacitor versus different current density

scan rates ranging from 5 mV/s to 100 mV/s are depicted in Figure 4D, which demonstrate an enlarged potential window of 1.15 V of asymmetric configuration. Two pairs of redox peaks can be clearly observed in these profiles, which are ascribed to the transitions between different redox states of PANI (leucoemeraldine base, emeraldine base, and pernigraniline base).[47] With the scan rate increasing from 5 to 100 mV/s, the redox peaks can still be traced, indicating the considerable rate capability of this ASC.[48] Galvanostatic charge or discharge (GCD) curves of the ASC recorded at different current densities, ranging from 1 to 10 mA/cm^2 based on the specific area of ASC, are exhibited in Figure 4E. It is noteworthy that the GCD profiles exhibit a distinct plateau located at 0.6–0.8 V, which is attributed to the pseudocapacitive characteristic of both CPH and MXene. Due to the high pseudocapacitance of the electrodes, the CPH//$Ti_3C_2T_x$ ASC delivers a large areal capacitance of 90.3 mF/cm^2 at a current density of 1 mA/cm^2. Even when the current density increases to 20 mA/cm^2, the areal capacitance can still be maintained at 43.4 mF/cm^2 (Supplementary Figure S11). Such a high areal capacitance surpasses most previous MXene-based supercapacitors and is comparative with many state-of-the-art works (Supplementary Figure S12).[12,13,16–18,20,23]

Sweep voltammetry can shed light into the charge storage kinetics of electrochemical procedure. To inspect the electrochemical kinetics for charge storage of as-assembled CPH//$Ti_3C_2T_x$ ASC, CV tests are conducted and analyzed using the power-law relationship (Equation 6):

$$i_p = av^b, \tag{6}$$

where i_p is the peak voltammetric current, v is the sweep rate, a and b are adjustable parameters. To point it out, $b = 0.5$ suggests a diffusion-controlled charge storage process, and $b = 1$ suggests a non-diffusion-controlled process (so-called capacitive behavior).[49] In Figure 4F, the $\log(i_p)$ versus $\log(v)$ plot for the anodic peak (0.74 V) and cathodic peak (0.66 V) shows the current dependence on the sweep rate. The b value for the anodic and cathodic peak current is calculated to be 0.78 and 0.83, respectively. From the perspective of b value, the charge stored in ASC is contributed by both diffusion-limited and non-diffusion-limited process.

To quantitatively distinguish capacitive contribution (non-diffusion-controlled) ratios at different scan rates, the following equation (Equation 7) can be effectively employed:

$$i(V) = k_1 v + k_2 v^{1/2}, \tag{7}$$

where $i(V)$ is current response at a fixed potential (V), v is the sweep rate, $k_1 v$ is described as the capacitive contribution, and $k_2 v^{1/2}$ is described as the diffusion-controlled insertion.[50] By determining the value of both k_1 and k_2, the fraction of each charge storage mechanism can be differentiated. As shown in Figure 4G and Supplementary Figure S13, the capacitive contribution (non-diffusion limited) is calculated to be 75% at 5 mV/s. With the scan rate increasing to 20 mV/s, the capacitive contribution increases to 83% correspondingly. The capacitive contribution analysis suggests that the non-diffusion limited charge storage mechanism plays the dominant role in the ASC. Notably, the small fraction of diffusion-controlled contribution can be ascribed to the ion intercalation into MXene lattice. Cyclic performance of as-prepared ASC is investigated by GCD technique at a fixed current density of 15 mA/cm^2. Even after 30,000 charge and discharge cycles, the ASC can well maintain its performance with no trackable capacitance decay (Supplementary Figure S14). Such a promising cyclic stability can be ascribed to the unblocked ion/mass transfer channels in both CPH and MXene electrode, which can mitigate the volume expansion/shrinkage effect during cycling. Notably, a distinct capacitance increment can be observed in the initial cyclic stage, which is attributed to the activation of electrode materials. On one hand, more active sites located on MXene flakes are exposed to electrolyte with cycling. On the other hand, the full swelling of the CPH is a time-consuming process. During the cycling process, more and more PANI polymeric chains become accessible to electrolyte due to the swelling of CPH. Therefore, the specific capacitance of CPH//$Ti_3C_2T_x$ ASC seems to be increased during the initial cycling stage. Interestingly, this phenomenon was also reported in previous works regarding MXene and CPs electrodes.[51,52] Energy density of CPH//$Ti_3C_2T_x$ ASC and $Ti_3C_2T_x$ symmetric supercapacitor (with the same MXene loading mass on each electrode) serving as reference device are depicted in Figure 4H. The ASC delivers a high energy density of 16.6 μWh/cm^2 at 0.6 mW/cm^2, which is 10 times the energy density of $Ti_3C_2T_x$ symmetric supercapacitor with the same loading mass (1.6 μWh/cm^2 at 0.3 mW/cm^2). The output of this ASC is also benchmarked with some recent works regarding MXene and CP-based supercapacitors (Supplementary Figure S15). As a result, the performance of the CPH//$Ti_3C_2T_x$ ASC outperforms many MXene and CP-based supercapacitors, and its performance is even comparable with some state-of-the-art works.[23,37,53–55] The remarkable improvement in energy density suggests that employing CPH cathode is an effective way toward high energy demand.

To verify the integratable potential of the CPH//$Ti_3C_2T_x$ ASC, the parallel and serial connecting ASC circuits were further fabricated and studied in detail. Figure 5A and B depicts the CV (20 mV/s) and GCD (galvanostatic current of 1 mA) curves of ASC unit, two ASCs serial connecting circuit, and three ASCs serial connecting circuit. By connecting ASCs in series, the potential window can be effectively broadened to 2.3 and 3.45 V. However, the voltametric current of serial circuits are recorded to be reduced compared with ASC unit because of the serial resistance. In Figure 5C, the equivalent series resistance (ESR) of serial circuit is found to be enhanced with the increasing number of ASC unit, which is consistent with the intrinsic characteristics of serial circuit. According to the fitted EIS data, an individual ASC unit can be regarded as electrical double-layer capacitance C_{dl} in parallel with a charge transfer resistance R_{ct}, and then the mentioned part in series with the ESR R_s and the faradaic pseudocapacitance C_F originated from PANI and MXene. As a result, the R_s containing electrode active materials resistance, electrolyte resistance, and interfaces resistance is calculated to be 3.9 Ω. The R_{ct} is fitted to be 1.2 Ω, indicating promising charge transfer dynamics (Supplementary Figure S16). CV curves of ASC unit and parallel circuits with fixed potential window of 0~1.15 V (shown in Figure 5D) indicate the output current can be correspondingly enlarged through parallel connecting. In comparison with ASC unit, the larger capacitance provided by parallel circuit is demonstrated by enduring much longer discharge time at a fixed discharge current (Figure 5E). By determining the x-intercept of the Nyquist plots (Figure 5F), the ESR of three ASCs parallel circuit (1.4 Ω) and two ASCs parallel circuit (1.9 Ω) are demonstrated to be much smaller than that of ASC unit (3.7 Ω). As a visualized demo, a "SWJTU" bulb panel containing 318 green LED bulbs can be successfully lightened by four

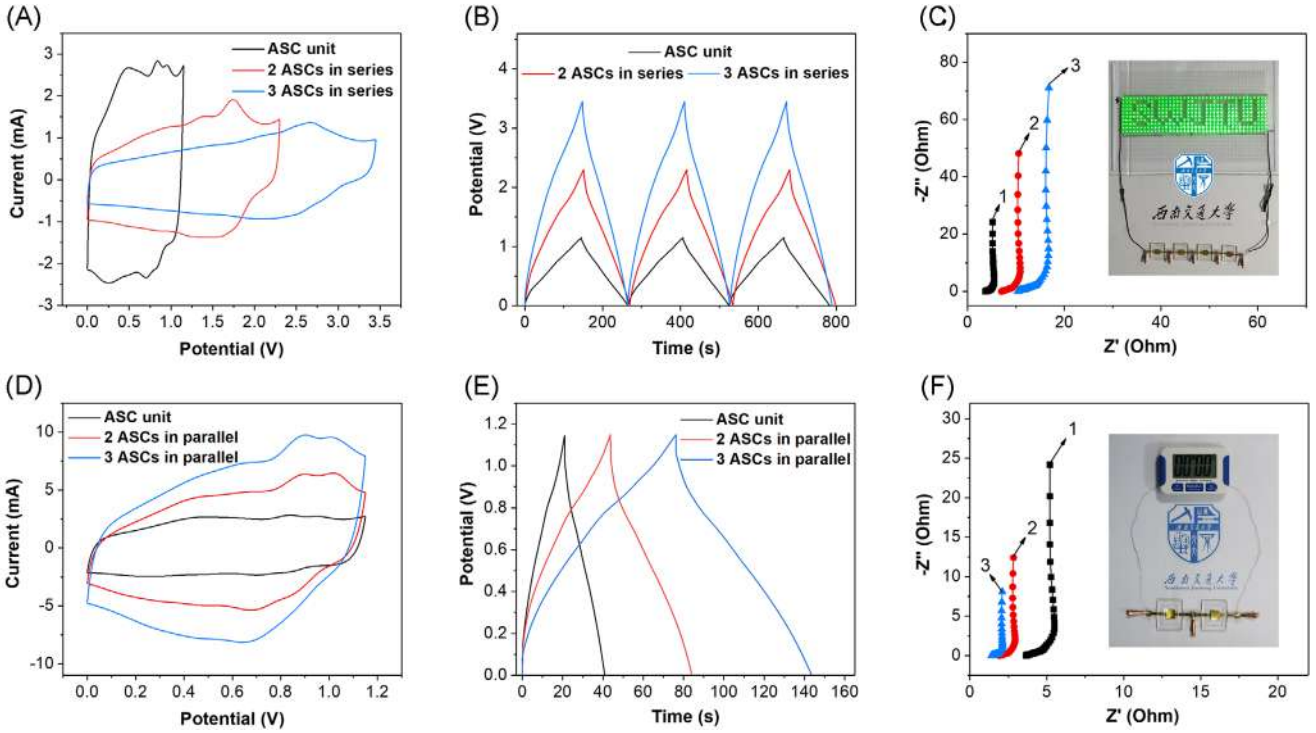

FIGURE 5 Electrochemical performance of different integrated CPH//$Ti_3C_2T_x$ ASC circuits. (A) CV curves, (B) GCD curves, and (C) EIS plots of ASC unit and serial ASC circuits. Inset picture of Figure 5C indicates 318 green LED bulbs can be effectively lightened by four ASCs serial circuits. (D) CV curves, (E) GCD curves, and (F) EIS plots of ASC unit and parallel ASC circuits. Inset picture in Figure 5F indicates an LCD timer can be successfully powered by two ASCs serial circuits

ASCs serial circuits (inset of Figure 5C), and a LCD timer can be easily powered by two ASCs serial circuits (inset of Figure 5F). The above-mentioned data unambiguously demonstrate that the $Ti_3C_2T_x$//CPH ASC can be used as a promising candidate for portable electronics and wearable devices in the approaching era of Internet of Things.

Through employing 3D CPH cathode and 2D $Ti_3C_2T_x$ anode, the ASC with a collection of merits, such as high energy density, large areal capacitance, and promising cyclic stability, can be elaborately fabricated. The above-mentioned merits of device should be mainly attributed to the following reasons: (i) The CPH shows high pseudocapacitance under positive potential in acidic electrolyte. It can thus match well with pseudocapacitive MXene ($Ti_3C_2T_x$) that works under negative potential. Consequently, the CPH//$Ti_3C_2T_x$ ASC exhibits promising comprehensive electrochemical performance. (ii) The highly interconnected 3D frameworks of CPH and large interlayer space of 2D MXene naturally form unblocked ion or mass transfer channels, which can give rise to efficient electrochemical dynamics. (iii) The considerable electronic conductivity of CPH and MXene electrode benefits electron transfer. As a result, good rate capability and cycling stability can be obtained. (iv) The synergistic effect between enhanced potential window and high pseudocapacitance of electrode materials make the device exploit its advantages to the full in acidic electrolyte. Therefore, the CPH//$Ti_3C_2T_x$ ASC shows remarkably enhanced energy density compared with symmetric MXene supercapacitor.

4 | CONCLUSIONS

In summary, we had elaborately designed the CPH with distinct 3D architectures via a supramolecular strategy, in which the PANI polymeric chains are efficiently crosslinked by CA molecules. The CPH positive electrode with promising pseudocapacitance can match well with pseudocapacitive $Ti_3C_2T_x$ negative electrode. Consequently, an aqueous ASC with enlarged potential window of 1.15 V can be successfully assembled. In the meanwhile, the CPH//$Ti_3C_2T_x$ ASC demonstrates remarkably enhanced energy density of 16.6 μWh/cm^2, which is nine times higher than that of aqueous symmetric $Ti_3C_2T_x$ supercapacitor. Additionally, the as-assembled ASC can be further integrated to drive different daily electronics such as LED scroll and LCD timer. In conclusion, this work sheds new lights into the synthesis of pseudocapacitive materials that match with $Ti_3C_2T_x$ negative electrode. It thus gives inspiration for the design of future MXene-based ASCs with enhanced energy density and application potential.

ACKNOWLEDGEMENTS

W.Y. and H.Z. acknowledges the National Natural Science Foundation of China (Nos. 51977185 and 51972277) and the Sichuan Science and Technology Program (Nos. 20ZDYF2478, 20ZDYF2833, and 21ZDYF3951). In addition, X.C. thanks the Analysis & Testing Center of Southwest Jiaotong University for SEM, TEM, and Raman characterizations.

CONFLICT OF INTEREST

The authors declare no conflict of interest.

DATA AVAILABILITY STATEMENT

The data that support the findings of this study are available from the corresponding author upon reasonable request.

ORCID

Weiqing Yang https://orcid.org/0000-0001-8828-9862

REFERENCES

1. VahidMohammadi A, Rosen J, Gogotsi Y. The world of two-dimensional carbides and nitrides (MXenes). *Science*. 2021;372:eabf1581.
2. Anasori B, Lukatskaya MR, Gogotsi Y. 2D metal carbides and nitrides (MXenes) for energy storage. *Nat Rev Mater*. 2017;2:16098.
3. Li K, Wang X, Wang X, et al. All-pseudocapacitive asymmetric MXene-carbon-conducting polymer supercapacitors. *Nano Energy*. 2020;75:104971.
4. Naguib M, Mochalin VN, Barsoum MW, Gogotsi Y. 25th anniversary article: mXenes: a new family of two-dimensional materials. *Adv Mater*. 2014;26:992-1005.
5. Li K, Wang X, Li S, et al. An ultrafast conducting polymer@MXene positive electrode with high volumetric capacitance for advanced asymmetric supercapacitors. *Small*. 2020;16:e1906851.
6. Wang Y, Wang X, Li X, et al. Engineering 3D ion transport channels for flexible MXene films with superior capacitive performance. *Adv Funct Mater*. 2019;29:1900326.
7. Xiong D, Li X, Bai Z, Lu S. Recent advances in layered Ti3C2Tx MXene for electrochemical energy storage. *Small*. 2018;14:e1703419.
8. Sun Y, Chen D, Liang Z. Two-dimensional MXenes for energy storage and conversion applications. *Mater Today Energy*. 2017;5:22-36.
9. Wang Y, Wang X, Li X, et al. Scalable fabrication of polyaniline nanodots decorated MXene film electrodes enabled by viscous functional inks for high-energy-density asymmetric supercapacitors. *Chem Eng J*. 2021;405:126664.
10. Xie Y, Zhang H, Huang H, et al. High-voltage asymmetric MXene-based on-chip micro-supercapacitors. *Nano Energy*. 2020;74:104928.
11. Ghidiu M, Lukatskaya MR, Zhao MQ, Gogotsi Y, Barsoum MW. Conductive two-dimensional titanium carbide 'clay' with high volumetric capacitance. *Nature*. 2014;516:78-81.
12. Huang H, Chu X, Su H, et al. Massively manufactured paper-based all-solid-state flexible micro-supercapacitors with sprayable MXene conductive inks. *J Power Sources*. 2019;415:1-7.
13. Peng YY, Akuzum B, Kurra N, et al. All-MXene (2D titanium carbide) solid-state microsupercapacitors for on-chip energy storage. *Energy Environ Sci*. 2016;9:2847-2854.
14. Zhang CJ, McKeon L, Kremer MP, et al. Additive-free MXene inks and direct printing of micro-supercapacitors. *Nat Commun*. 2019;10:1795.
15. Wen D, Ying GB, Liu L, et al. Flexible and high-performance MXene/MnO_2 film electrodes fabricated by inkjet printing: toward a new generation supercapacitive application. *Adv Mater Interfaces*. 2021;8:2101453.
16. Ma J, Zheng S, Cao Y, et al. Aqueous MXene/PH1000 hybrid inks for inkjet-printing micro-supercapacitors with unprecedented volumetric capacitance and modular self-powered microelectronics. *Adv Energy Mater*. 2021;11:2100746.
17. Yu L, Fan Z, Shao Y, Tian Z, Sun J, Liu Z. Versatile N-doped MXene ink for printed electrochemical energy storage application. *Adv Energy Mater*. 2019;9:1901839.
18. Abdolhosseinzadeh S, Schneider R, Verma A, Heier J, Nuesch F, Zhang CJ. Turning trash into treasure: additive free MXene sediment inks for screen-printed micro-supercapacitors. *Adv Mater*. 2020;32:e2000716.
19. Orangi J, Hamade F, Davis VA, Beidaghi M. 3D Printing of Additive-free 2D Ti_3C_2Tx (MXene) ink for fabrication of micro-supercapacitors with ultra-high energy densities. *ACS Nano*. 2020;14:640-650.
20. Li X, Li H, Fan X, Shi X, Liang J. 3D-printed stretchable micro-supercapacitor with remarkable areal performance. *Adv Energy Mater*. 2020;10:1903794.
21. Das P, Wu ZS. MXene for energy storage: present status and future perspectives. *J Physics:Energ*. 2020;2:032004.
22. Wang Z, Xu Z, Huang H, et al. Unraveling and regulating self-discharge behavior of Ti3C2Tx MXene-based supercapacitors. *ACS Nano*. 2020;14:4916-4924.
23. Zhang CJ, Kremer MP, Seral-Ascaso A, et al. Stamping of flexible, coplanar micro-supercapacitors using MXene inks. *Adv Funct Mater*. 2018;28:1705506.
24. Dong Y, Shi H, Wu ZS. Recent advances and promise of MXene-based nanostructures for high-performance metal ion batteries. *Adv Funct Mater*. 2020;30:2000706.
25. Huang H, He J, Wang Z, et al. Scalable, and low-cost treating-cutting-coating manufacture platform for MXene-based on-chip micro-supercapacitors. *Nano Energy*. 2020;69:104431.
26. Lv J, Chen J, Lee PS. Sustainable wearable energy storage devices self-charged by human-body bioenergy. *SusMat*. 2021;1:285-302.
27. Zhang X, Lin H, Shang H, Xu J, Zhu J, Huang W. Recent advances in functional fiber electronics. *SusMat*. 2021;1:105-126.
28. Zhang H, Zhang L, Chen J, Su H, Liu F, Yang W. One-step synthesis of hierarchically porous carbons for high-performance electric double layer supercapacitors. *J Power Sources*. 2016;315:120-126.
29. Couly C, Alhabeb M, Van Aken KL, et al. Asymmetric flexible MXene-reduced graphene oxide micro-supercapacitor. *Adv Electron Mater*. 2017;4:1700339.
30. Boota M, Gogotsi Y. MXene-conducting polymer asymmetric pseudocapacitors. *Adv Energy Mater*. 2018;9:1802917.

31. Jiang Y, Guo F, Liu Y, Xu Z, Gao C. Three-dimensional printing of graphene-based materials for energy storage and conversion. *SusMat*. 2021;1:304-323.
32. Su H, Huang H, Zhang H, et al. In situ direct method to massively prepare hydrophilic porous carbide-derived carbons for high-performance supercapacitors. *ACS Appl Energy Mater*. 2018;1:3544-3553.
33. Su H, Huang H, Zhao S, et al. Understanding the ion-sorption dynamics in functionalized porous carbons for enhanced capacitive energy storage. *ACS Appl Mater Interfaces*. 2020;12:2773-2782.
34. Zhao Y, Liu B, Pan L, Yu G. 3D nanostructured conductive polymer hydrogels for high-performance electrochemical devices. *Energy Environ Sci*. 2013;6:2856-2870.
35. Pan L, Yu G, Zhai D, et al. Hierarchical nanostructured conducting polymer hydrogel with high electrochemical activity. *P Natl Acad Sci*. 2012;109:9287-9292.
36. Wang Q, Zhou Y, Zhao X, et al. Tailoring carbon nanomaterials via a molecular scissor. *Nano Today*. 2021;36:101033.
37. Chu X, Huang H, Zhang H, et al. Electrochemically building three-dimensional supramolecular polymer hydrogel for flexible solid-state micro-supercapacitors. *Electrochim Acta*. 2019;301:136-144.
38. Li WW, Gao FX, Wang XQ, Zhang N, Ma MM. Strong and robust polyaniline-based supramolecular hydrogels for flexible supercapacitors. *Angew Chem Int Edit*. 2016;55:9196-9201.
39. Wang Y, Shi Y, Pan L, et al. Dopant-enabled supramolecular approach for controlled synthesis of nanostructured conductive polymer hydrogels. *Nano Lett*. 2015;15:7736-7741.
40. Shi Y, Pan L, Liu B, et al. Nanostructured conductive polypyrrole hydrogels as high-performance, flexible supercapacitor electrodes. *J Mater Chem A*. 2014;2:6086-6091.
41. Chu X, Chen G, Xiao X, et al. Air-stable conductive polymer ink for printed wearable micro-supercapacitors. *Small*. 2021:e2100956.
42. Zhang C, Allioux FM, Rahim MA, et al. Nucleation and growth of polyaniline nanofibers onto liquid metal nanoparticles. *Chem Mater*. 2020;32:4808-4819.
43. Du F, Tang H, Pan L, et al. Environmental friendly scalable production of colloidal 2d titanium carbonitride mxene with minimized nanosheets restacking for excellent cycle life lithium-ion batteries. *Electrochim Acta*. 2017;235:690-699.
44. Shuck CE, Sarycheva A, Anayee M, et al. Scalable synthesis of Ti_3C_2Tx MXene. *Adv Eng Mater*. 2020;22:1901241.
45. Sarycheva A, Gogotsi Y. Raman spectroscopy analysis of the structure and surface chemistry of Ti_3C_2Tx MXene. *Chem Mater*. 2020;32:3480-3488.
46. Zhang L, Su W, Huang Y, et al. In situ high-pressure x-ray diffraction and raman spectroscopy study of Ti_3C_2Tx MXene. *Nanoscale Res Lett*. 2018;13:343.
47. Chu X, Zhu Z, Huang H, et al. Conducting polymer ink for flexible and printable micro-supercapacitors with greatly-enhanced rate capability. *J Power Sources*. 2021;513:230555.
48. Wang Y, Chu X, Zhu Z, Xiong D, Zhang H, Yang W. Dynamically evolving 2D supramolecular polyaniline nanosheets for long-stability flexible supercapacitors. *Chem Eng J*. 2021;423:130203.
49. Brezesinski T, Wang J, Tolbert SH, Dunn B. Ordered mesoporous α-MoO_3 with iso-oriented nanocrystalline walls for thin-film pseudocapacitors. *Nat Mater*. 2010;9:146-151.
50. Kim HS, Cook JB, Lin H, et al. Oxygen vacancies enhance pseudocapacitive charge storage properties of MoO_3−x. *Nat Mater*. 2016;16:454-460.
51. Chu X, Zhao X, Zhou Y, et al. An ultrathin robust polymer membrane for wearable solid-state electrochemical energy storage. *Nano Energy*. 2020;76:105179.
52. Zheng S, Wang H, Das P, et al. Multitasking MXene inks enable high-performance printable microelectrochemical energy storage devices for all-flexible self-powered integrated systems. *Adv Mater*. 2021;33:e2005449.
53. Huang P, Lethien C, Pinaud S, et al. On-chip and freestanding elastic carbon films for micro-supercapacitors. *Science*. 2016;351:691-695.
54. Liu WW, Feng YQ, Yan XB, Chen JT, Xue QJ. Superior micro-supercapacitors based on graphene quantum dots. *Adv Funct Mater*. 2013;23:4111-4122.
55. Liu WW, Lu CX, Li HL, et al. Paper-based all-solid-state flexible micro-supercapacitors with ultra-high rate and rapid frequency response capabilities. *J Mater Chem A*. 2016;4:3754-3764.

SUPPORTING INFORMATION

Additional supporting information may be found in the online version of the article at the publisher's website.

How to cite this article: Chu X, Wang Y, Cai L, et al. Boosting the energy density of aqueous MXene-based supercapacitor by integrating 3d conducting polymer hydrogel cathode. *SusMat*. 2022;1-12. https://doi.org/10.1002/sus2.61